

Nanoscale

Accepted Manuscript



This is an *Accepted Manuscript*, which has been through the Royal Society of Chemistry peer review process and has been accepted for publication.

Accepted Manuscripts are published online shortly after acceptance, before technical editing, formatting and proof reading. Using this free service, authors can make their results available to the community, in citable form, before we publish the edited article. We will replace this *Accepted Manuscript* with the edited and formatted *Advance Article* as soon as it is available.

You can find more information about *Accepted Manuscripts* in the [Information for Authors](#).

Please note that technical editing may introduce minor changes to the text and/or graphics, which may alter content. The journal's standard [Terms & Conditions](#) and the [Ethical guidelines](#) still apply. In no event shall the Royal Society of Chemistry be held responsible for any errors or omissions in this *Accepted Manuscript* or any consequences arising from the use of any information it contains.

A Facile Solvent Vapor Fumigation Induced Self-repair Recrystallization of $\text{CH}_3\text{NH}_3\text{PbI}_3$ Films for High Performance Perovskite Solar Cells

Weidong Zhu,^a Tao Yu,^{*abc} Faming Li,^a Chunxiong Bao,^a Hao Gao,^a Yong Yi,^a Jie Yang,^a Gao Fu,^a

Xiaoxin Zhou^a and Zhigang Zou^{abc}

ABSTRACT

A high quality $\text{CH}_3\text{NH}_3\text{PbI}_3$ film is crucial for a high performance perovskite solar cell. Here, a recrystallization process via facile fumigation of DMF vapor has been successfully introduced to self-repair of $\text{CH}_3\text{NH}_3\text{PbI}_3$ films with poor coverage and low crystallinity prepared by the commonly used one-step spin-coating method. It is found that the $\text{CH}_3\text{NH}_3\text{PbI}_3$ films with dendritic structures can spontaneously transform to the uniform ones with full coverage and high crystallinity by adjusting the cycles of the recrystallization process. The mesostructured perovskite solar cells based on these repaired $\text{CH}_3\text{NH}_3\text{PbI}_3$ films showed the reproducible optimal power conversion efficiency (PCE) of 11.15% and the average PCE of $10.25 \pm 0.90\%$, which are much better than that of the devices based on the non-repaired $\text{CH}_3\text{NH}_3\text{PbI}_3$ films. In addition, the hysteresis phenomenon in the current-voltage test can also be effectively alleviated due to the quality of the films being improved in the optimized devices. Our work proved that the fumigation of solvent vapor can modify the metal organic perovskite films such as $\text{CH}_3\text{NH}_3\text{PbI}_3$. It offers a novel and attractive way to fabricate high performance perovskite solar cells.

1. Introduction

As the important members of the next-generation photovoltaic (PV) devices,

dye-sensitized solar cells (DSSCs),¹ organic bulk heterojunction solar cells,² and colloidal nanocrystal solar cells,³ have attracted much interest during the past decades since they can be assembled with low-cost materials and cost-effective methods.^{4,5} As a new kind of PV devices derived from DSSCs, perovskite solar cells have recently become the rapidly rising stars due to their swiftly increased power conversion efficiency (PCE) up to 20.1% from 3.8%.^{6,7} The metal organic perovskite materials such as $\text{CH}_3\text{NH}_3\text{PbI}_3$ are the most important components in the cells. They have their unique features as follows, 1) excellent and tunable optical properties with the change of chemical compositions;^{8,9} 2) long carrier diffusion lengths (100~1000 nm) and long lifetimes (~100 ns) due to their large dielectric coefficients;^{10,11} 3) ambipolar charge transport properties;¹² 4) low temperature (<100 °C) solution processability due to a self-assembly driven phase transformation.^{9,13,14} All these merits are vital for their applications in the high performance PV devices.^{15,16}

In order to play their excellent characteristics effectively in the high performance PV devices, numerous efforts have been focused on the preparation of high quality metal organic perovskite films because the poor morphology and low crystallinity of the films not only cause the electrical shorting but also deleteriously impact the charge dissociation/transport/recombination in the devices.^{4,15,17,18} Most of them based on engineering the films' nucleation and growth processes, including one-step spin-coating,¹⁹ sequential deposition from solution,²⁰ dual-source vapor evaporation,²¹ and vapor-assisted solution process.²² Among them, the one-step spin-coating is the most widely used one.²³ But it is difficult to yield a homogeneous metal organic

perovskite film with uniform and full coverage in large areas.^{4, 23} Some effective modifications have been done to this method. For example, Cheng et al. fabricated flat and uniform $\text{CH}_3\text{NH}_3\text{PbI}_3$ films by exposing the spin-coated precursor film in a second solvent or dry Ar gas stream and realized the devices with the PCE > 13%.^{4, 24} Dense $\text{CH}_3\text{NH}_3\text{PbI}_3$ films were also obtained by introducing additives, such as 1,8-diiodooctane,¹⁵ $\text{CH}_3\text{NH}_3\text{Cl}$,²⁵ and NH_4Cl ²⁶ in the precursor solution. Recently, solvent engineering techniques were also developed to produce very uniform $\text{CH}_3\text{NH}_3\text{Pb}(\text{I}_{1-x}\text{Br}_x)_3$ films by one-step spin-coating method, and enabled the fabrication of solar cells with the certified PCE of 16.2%.²³

Complementary to directly engineering the nucleation and growth processes in the synthesis stage of films, the post treatment on the synthesized films has also been regarded as an effective way to tailor the physical and chemical properties of inorganic and organic films. In particular, it has been reported that the post-synthesis treatments can induce the recrystallization of active layers of thin film solar cells, thus significantly improving their morphology and crystallinity, as well as the device performances. For example, recrystallization of CdTe films under various condition including high temperature, mechanical pressure, and CdCl_2 treatment can facilitate the growth of CdTe grains, and as a consequence the efficiency of the devices can be enhanced.²⁷⁻²⁹ The morphology improvement of CuInS_2 thin films after recrystallization was also verified in the previous studies.³⁰⁻³² Meanwhile, it has been demonstrated that the solvent vapor fumigation was an effective method to promote the crystallization of some special organics, such as vanadyl phthalocyanine dyes,³³

syndiotactic polystyrene,³⁴ and polycarbonate of bisphenol A,³⁵ etc.. It means that recrystallization of the one-step spin-coated perovskite films by a post-synthesis treatment such as solvent vapor fumigation can modify the films' morphologies and crystallinities.

In this study, a recrystallization process via facile DMF vapor fumigation has been successfully introduced to self-repair of the one-step spin-coated $\text{CH}_3\text{NH}_3\text{PbI}_3$ films with dendritic structures to the uniform ones with full coverage and high crystallinity. The mesostructured perovskite solar cells based on these repaired $\text{CH}_3\text{NH}_3\text{PbI}_3$ films showed the reproducible optimal PCE of 11.15% and the average PCE of $10.25 \pm 0.90\%$, which are much better than that of the devices based on the non-repaired $\text{CH}_3\text{NH}_3\text{PbI}_3$ films. In addition, the hysteresis phenomenon in the J-V test can also be effectively alleviated due to the quality of the $\text{CH}_3\text{NH}_3\text{PbI}_3$ films being improved in the optimized devices.

2. Experimental Section

2.1 Materials

Hydroiodic acid (57 wt % in water) and methylamine (33 wt% in absolute ethanol) were purchased from Sigma-Aldrich. Li-bis-(trifluoromethanesulfonyl) imide (Li-TFSI, 98%), 4-tert-butylpyridine (TBP, 98%), dimethylformamide (DMF, anhydrous 99.5%) and lead iodide (PbI_2 , 99.999%) were purchased from Aladdin Reagents. Tetrabutyl titanate, acetonitrile, chlorobenzene, diethanolamine, and isopropanol were purchased from Sinopharm Chemical Reagent Co., Ltd. (China). 2,2',7,7'-tetrakis (N,N-di-p-methoxy-phenylamine)-9,9'-spirobifluorene

(Spiro-MeOTAD, $\geq 99\%$) was purchased from Shenzhen Feiming Science and Technology Co., Ltd. (China). All of the used reagents were analytical grade, without further purification.

2.2 Solar cell fabrication

Preparation of the mesoporous TiO₂ films: Patterned fluorine-doped tin oxide (FTO) glass substrates with sheet resistance of $14 \Omega \text{ sq}^{-1}$ were cleaned by ultrasonic washing in detergent solution, acetone, absolute alcohol, and deionized water for 20 min each in succession, and then treated by UV-ozone cleaning for 30 min. TiO₂ sol was dropped onto the pre-cleaned substrates to form compact TiO₂ layers with the thickness of about 100 nm by spin-coating at 3000 rpm for 30 s, and followed by annealing at 450 °C for 40 min in air. TiO₂ paste (Dyesol 18NR-T) diluted with ethanol at 1:3.5 by weight was then dropped onto the TiO₂ compact film to form mesoporous TiO₂ layer with the thickness of about 400 nm by spin-coating at 3000 rpm for 30 s, followed by annealing at 500 °C for 30 min in air.

Preparation of the CH₃NH₃PbI₃ films and recrystallization via DMF vapor fumigation: First, CH₃NH₃I was synthesized according to the recipe reported by Lee et al.¹² Then, PbI₂ and CH₃NH₃I with molar ratio of 1:1 were mixed in DMF and stirred at room temperature for 12 h to form the 40 wt% CH₃NH₃PbI₃ precursor solution. Next, the solution was dropped onto the mesoporous TiO₂ films to prepare the sample CH₃NH₃PbI₃ films by spin-coating at 2500 rpm for 30 s, followed by annealing at 90 °C for 10 min in the dry box with relative humidity below 10%. Thus, the sample CH₃NH₃PbI₃ films with black color were obtained. In the recrystallization process via

DMF vapor fumigation, the prepared sample $\text{CH}_3\text{NH}_3\text{PbI}_3$ films were put on the top of a hot plate pre-heated at $90\text{ }^\circ\text{C}$ in the dry box and carpeted with a filter paper. A portion of 0.5 mL DMF solution was then dropped onto the filter paper, and quickly covered with a culture dish to form the DMF vapor atmosphere. The black $\text{CH}_3\text{NH}_3\text{PbI}_3$ samples gradually turned pale yellow from edges toward center in about 2 s , indicating the dissolution of $\text{CH}_3\text{NH}_3\text{PbI}_3$ in DMF vapor atmosphere. After being fumigated for about 10 s , they were transferred to another hot plate pre-heated at $90\text{ }^\circ\text{C}$ and annealed for 10 min in dry box. The $\text{CH}_3\text{NH}_3\text{PbI}_3$ films were recrystallized from the DMF vapor and the color of the samples gradually returned to black. The above recrystallization procedure was exactly controlled and continuously repeated for $2, 4, 6, 10$ cycles, and the corresponding samples were labeled as C2, C4, C6, and C10, respectively. The sample without the recrystallization treatment was also prepared and labeled as C0 for comparison. The above experiment processes for the preparation of $\text{CH}_3\text{NH}_3\text{PbI}_3$ films and recrystallization via DMF vapor fumigation are also schematically shown in Figure 1.

Fabrication of the devices: 72.3 mg spiro-MeOTAD, $17.5\text{ }\mu\text{L}$ lithium Li-TFSI in acetonitrile (500 mg/mL) and $28.8\text{ }\mu\text{L}$ TBP were mixed in 1 mL chlorobenzene to form the hole transport material (HTM) solution. Then, the solution was coated on the $\text{CH}_3\text{NH}_3\text{PbI}_3$ samples to form HTM layer by spin-coating at 2500 rpm for 30 s . After being preserved in dark in dry box for 24 h , Ag counter electrode with the thickness of about 100 nm and the area of 0.28 cm^2 was deposited on the top HTM layer by thermal evaporation technique. Thus, the mesostructured perovskite solar cells with

the configuration of FTO/ compact-TiO₂/ mesoporous-TiO₂ / CH₃NH₃PbI₃/ spiro-MeOTAD/Ag were fabricated to further characterize their cell properties.

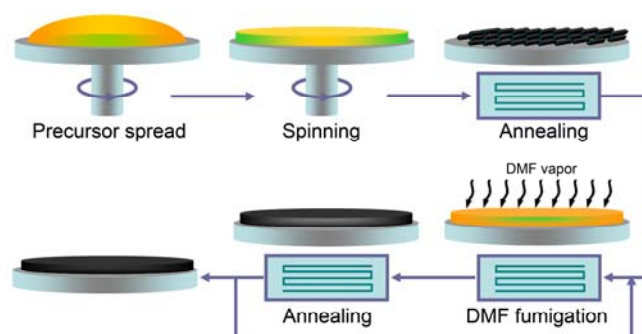


Figure 1 schematic procedure for the preparation of the CH₃NH₃PbI₃ film and recrystallization via DMF vapor fumigation.

2.3 Characterizations

A FEI NOVA NanoSEM230 scanning electron microscopy (SEM) was employed to characterize the morphological properties of the samples. X-Ray diffraction (XRD) patterns were collected on a Rigaku Ultima III X-ray diffractometer (Cu K α) in the range of 10^o-60^o. A Shimadzu UV-2550 UV-vis spectrometer fitted with an integrating sphere was used to investigate the absorption properties of the samples. Time-resolved photoluminescence (PL) decay property was obtained using the time-correlated single-photon counting technique (PicoHarp 300). The samples were photoexcited using a laser beam pulsed at 5 MHz. The performance measurements of the fabricated solar cells were carried on a Keithley 2400 source measurement unit under AM1.5 illumination (standard 100 mW cm⁻²) cast by an Oriel 92251A-1000 sunlight simulator calibrated by the standard reference of a Newport silicon solar cell. A black mask with a circular aperture (0.07 cm²) was applied on top of the solar cell. The incident photon conversion efficiency (IPCE) was measured using a 150 W xenon

lamp (Oriol) fitted with a monochromator (Cornerstone 74004) as a monochromatic light source.

3. Results and Discussion

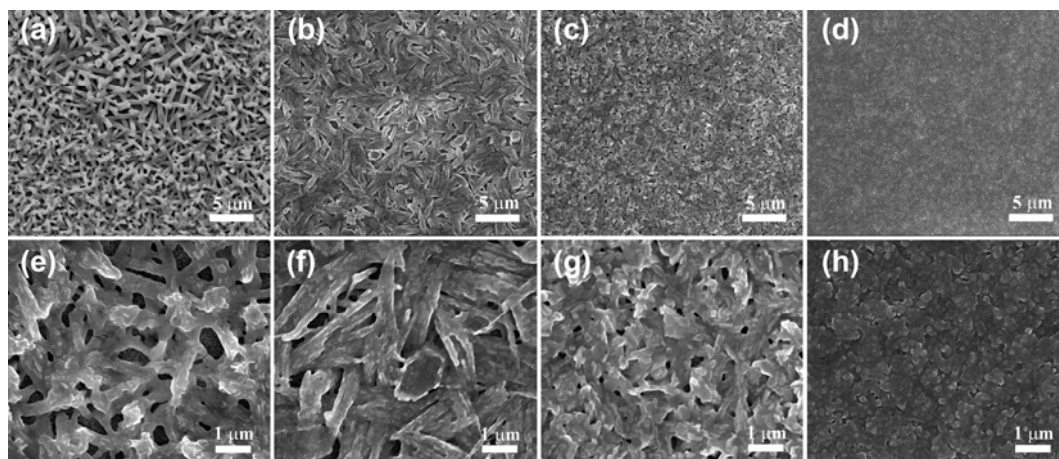


Figure 2 Surface SEM images of the samples C0 (a, e), C2 (b, f), C4 (c, g), and C6 (d, h), respectively.

The morphology of the samples C0, C2, C4, and C6 were analyzed by SEM, and the corresponding results are shown in Figure 2. As revealed in Figure 2(a)-(d), each of the $\text{CH}_3\text{NH}_3\text{PbI}_3$ films has a unique morphology in a large scale, which benefits from the inherent characters of spin-coating method and the following DMF vapor fumigation. By comparison, the surface roughness of the $\text{CH}_3\text{NH}_3\text{PbI}_3$ films after recrystallization is significantly decreased, which become more evident with the increase of the recrystallization cycle. To further reveal the morphology details of the $\text{CH}_3\text{NH}_3\text{PbI}_3$ films, high-resolution SEM images are given in Figure 2(e)-(h). It can be seen that the $\text{CH}_3\text{NH}_3\text{PbI}_3$ film prepared by the one-step spin-coating method is in the poor dendritic structure covering the mesoporous TiO_2 layer, which is consistent with the previous studies.²⁴ As expected, the $\text{CH}_3\text{NH}_3\text{PbI}_3$ films exhibit strikingly different morphologies after recrystallization. For the sample C2, the dendritic

$\text{CH}_3\text{NH}_3\text{PbI}_3$ structures start to widen and flatten, which is accompanied by the increase of the film coverage. When the recrystallization cycle was increased to four, the dendritic $\text{CH}_3\text{NH}_3\text{PbI}_3$ structures seem to be completely disappeared, as a result of the formation of randomly packed $\text{CH}_3\text{NH}_3\text{PbI}_3$ grains with interconnected crystalline grain networks. Yet, there are still some pinholes sparsely dispersing on the surface. By increased the recrystallization cycle to six, the $\text{CH}_3\text{NH}_3\text{PbI}_3$ film exhibits a dense grained uniform morphology. Obviously, the coverage and quality of the $\text{CH}_3\text{NH}_3\text{PbI}_3$ films improve with the increase of the recrystallization cycle. So we further repeated this process for ten cycles, yet it is found that the edges of the $\text{CH}_3\text{NH}_3\text{PbI}_3$ film shrink seriously, which exhibits distinct morphology compared with the film center, as revealed in Figure S1. The non-uniformity may detrimentally affect the reproducibility of the ultimate PV devices,¹⁷ so our works were mainly focused on the samples of less than 6 recrystallization cycles.

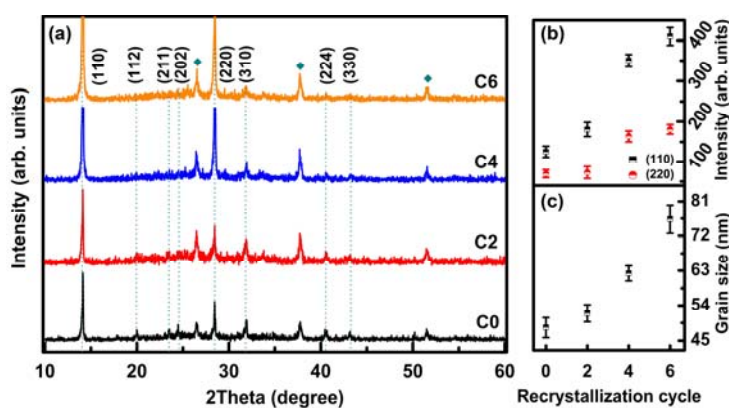


Figure 3 (a) XRD patterns from the samples C0, C2, C4, and C6, respectively. The diamond symbol denotes the signals from the substrate. (b) The intensities of diffraction peaks corresponding to the (110) and (220) lattice planes of $\text{CH}_3\text{NH}_3\text{PbI}_3$ films. (c) The corresponding average crystallite size of the samples, which was calculated based on the Scherrer Equation using the value of full widths at half maximum of the diffraction peak of the (110) plane. The horizontal ordinate of 0, 2, 4, and 6 in (b) and (c) represents the samples C0, C2, C4, and C6, respectively.

XRD measurements were conducted to investigate whether the morphology evolution would affect the crystal structure of the $\text{CH}_3\text{NH}_3\text{PbI}_3$ films. As shown in Figure 3, all the samples show the major diffraction peaks of the perovskite phase of $\text{CH}_3\text{NH}_3\text{PbI}_3$, which is indicated by the dominant peaks located at 14.08° , 28.40° , and 31.86° , corresponding to the (110), (220), and (310) lattice planes, respectively.^{14, 25} Comparing to sample C0, both diffraction peaks of (110) and (220) lattice planes of samples C2, C4, and C6 become higher in sequence as shown in Figure 3(b), which reveals that both of the film crystallinity and the growth of grains (as revealed in Figure 3(c)) can be improved with the increase of the recrystallization cycle.³⁶ Moreover, the small diffraction peaks of (112), (211), and (202) planes, related to the randomly oriented $\text{CH}_3\text{NH}_3\text{PbI}_3$ crystal domains, are significantly weakened for the samples C2, C4, and C6.³⁷ All results imply the film crystallinity can become better after the controlled recrystallization, which is in accordance with the results in Figure 2. In addition, the characteristic peaks of PbI_2 or $\text{CH}_3\text{NH}_3\text{I}$ are not observed in the samples C2, C4 and C6, indicating that the possible phase separation or decomposition of the $\text{CH}_3\text{NH}_3\text{PbI}_3$ films is avoided during the recrystallization process. These characters are beneficial to both the performance and the reproducibility of the ultimate PV devices.³⁸

Figure 4 gives the UV-vis absorption spectra of the samples C0, C2, C4, and C6.

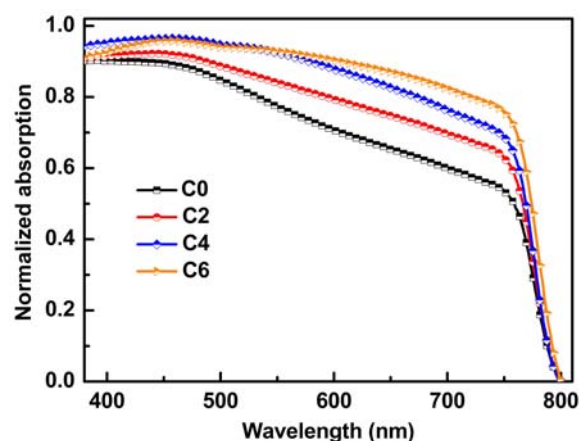


Figure 4 Normalized UV-vis absorption spectra of the samples C0, C2, C4, and C6, respectively, which are calculated from the corresponding measured transmittance and reflectance spectra shown in Figure S2.

It is obvious that all the samples exhibit a panchromatic absorption of light with spectra extended over the visible to near infrared region, which is consistent with the previous studies.^{8, 39} Impressively, the samples C2, C4, and C6 show the enhanced light harvesting in the wavelength range of 550-800 nm compared with the sample C0, which become more evident with the increase of the recrystallization cycle. Such an enhancement is mainly related to the combined effects of the improved coverage and crystallinity of the $\text{CH}_3\text{NH}_3\text{PbI}_3$ films after recrystallization.

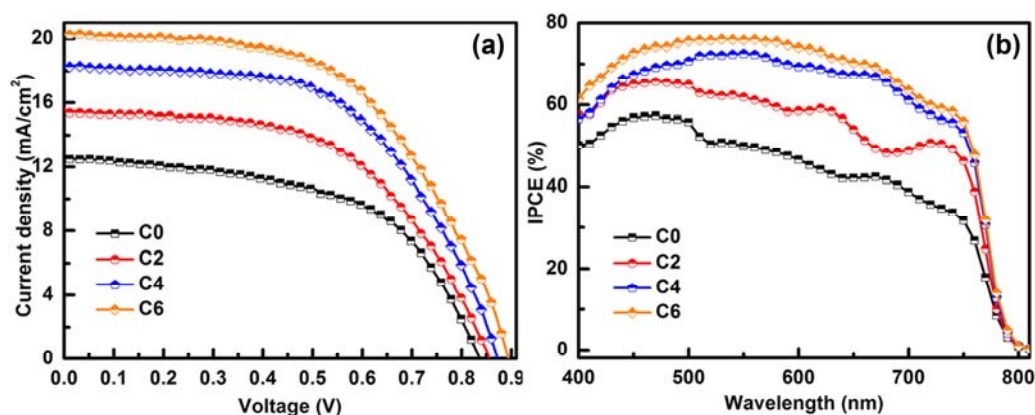


Figure 5 (a) J-V curves of the devices based on the samples of C0, C2, C4, and C6, respectively. The voltage scan direction was from forward bias to short circuit for all the devices. (b) IPCE spectra of devices fabricated with the samples of C0, C2, C4, and C6, respectively.

We further evaluated the effects of the coverage and the crystallinity enhancements of the $\text{CH}_3\text{NH}_3\text{PbI}_3$ films on the performance of the perovskite solar cells by employed the device configuration of FTO / compact TiO_2 / mesoporous TiO_2 / $\text{CH}_3\text{NH}_3\text{PbI}_3$ / spiro-MeOTAD / Ag. The current density-voltage (J-V) curves of the solar cells with the samples C0, C2, C4, and C6 measured under simulated AM1.5 (100 mW cm^{-2}) illumination are presented in Figure 5(c). It can be seen that the device with the sample C0 exhibits the short circuit current density (J_{sc}), the open circuit voltage (V_{oc}), the fill factor (FF), and the PCE to be 12.46 mA cm^{-2} , 0.83 V , 0.49 , and 5.07% , respectively. These inferior performance characteristics can be ascribed to the poor coverage and the low crystallinity of sample C0.^{15, 17} In contrast, for the devices used the samples C2, C4, and C6, the J_{sc} are 15.62 , 18.43 , and 20.12 mA cm^{-2} , and the corresponding PCE are 7.28% , 8.93% , and 10.16% , respectively. Clearly, the performance of the solar cells containing the $\text{CH}_3\text{NH}_3\text{PbI}_3$ films after recrystallization is significantly improved, and can be optimized by adjusting the recrystallization cycle.

Table 1 The PV parameters of the perovskite solar cells assembled with the samples C0, C2, C4, and C6, respectively.

Samples	J_{sc} (mA cm^{-2})	V_{oc} (V)	FF	PCE (%)
C0	12.46	0.83	0.49	5.07
C2	15.62	0.85	0.54	7.28
C4	18.43	0.87	0.56	8.93
C6	20.12	0.89	0.57	10.16

The photoelectric conversion characteristics of the fabricated devices were further investigated by measuring their IPCE, which is defined as the number of photogenerated charge carriers contributing to the photocurrent per incident photon.⁴⁰

As revealed in Figure 5(d), the photocurrent generation starts at around 800 nm, in agreement with the reported band gap of perovskite $\text{CH}_3\text{NH}_3\text{PbI}_3$ materials (1.55 eV).⁸ All the IPCE spectra reach a maximum value at ~500 nm, and then decrease from 600 nm, indicating a photocurrent loss due to either insufficient absorption of the $\text{CH}_3\text{NH}_3\text{PbI}_3$ layer or the optical interference.⁴⁰ The device with the sample C0 exhibited the IPCE below 60%, while the devices with the samples C2, C4, and C6 show the remarkable improvements of photocurrent over the whole region. Especially, for the device with the sample C6 the IPCE maximum can reach about 76%. These results match the differences of J_{sc} values for the devices with the samples C0, C2, C4, and C6.

Many factors can affect the performance of perovskite solar cells. It is always difficult to determine the exact contribution of each factor due to their possible relevance and also the absence of direct characterizations for some potential factors. However, it is still necessary and also desirable to follow some key points to understand the greatly enhanced PCE with the $\text{CH}_3\text{NH}_3\text{PbI}_3$ films after recrystallization based on our currently obtained information. Compared with the device with the sample C0, the differences only consist in the $\text{CH}_3\text{NH}_3\text{PbI}_3$ layers for the devices with the samples C2, C4, and C6. Therefore, the properties determined by the modifications of the $\text{CH}_3\text{NH}_3\text{PbI}_3$ films' morphology and crystallinity can be responsible for the greatly enhanced PV properties. On one hand, the improved coverage of the $\text{CH}_3\text{NH}_3\text{PbI}_3$ films after recrystallization is a vital factor should to be reckoned.^{23, 24} The reasons for ensuring the film coverage are two-folds: firstly, if

there are regions without $\text{CH}_3\text{NH}_3\text{PbI}_3$ padding, light will directly pass through without absorption, thus decreasing the available photocurrent; secondly, any insufficient coverage easily results in the formation of low resistance shutting paths allowing the direct contact of HTM layer with mesoporous TiO_2 layer.⁴¹ Any such path will act as a parallel resistor in the solar cell equivalent circuit, causing the drops of V_{oc} , FF, and PCE.³⁸ As exhibited in Figure 2, compared with the sample C0, the coverage of samples C2, C4 and C6 improved with the increasing of the recrystallization cycle; therefore, the enhancements of J_{sc} , V_{oc} , and FF of the corresponding devices follow the same trend.

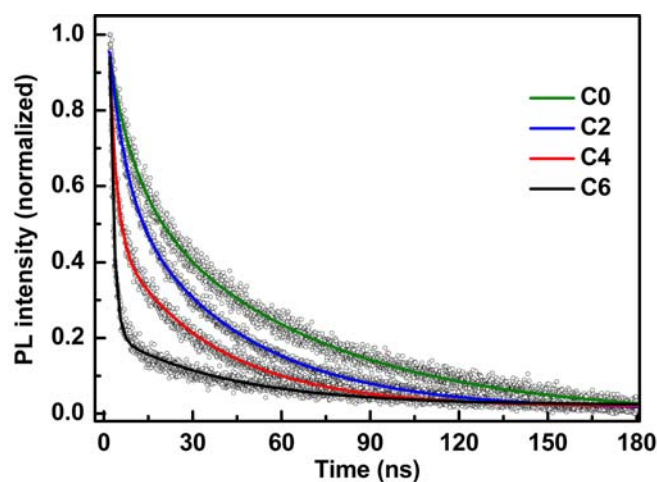


Figure 6 Normalized time-resolved PL decay curves detected at the peak emission wavelength of 780 nm for the samples C0, C2, C4, and C6, respectively.

Table 2 Summary of the biexponential fit decay parameters for the PL decays shown in Figure 6.

Samples	τ_{fast} (ns)	Fraction _{fast}	τ_{slow} (ns)	Fraction _{slow}
C0	8.8	37%	61.9	63%
C2	5.7	42%	41.3	58%
C4	2.4	66%	34.2	34%
C6	1.4	92%	31.0	8%

On the other hand, the decrease of defects resulted from the improvement of film crystallinity is another important aspect. It has been demonstrated that the decrease of

defects in the $\text{CH}_3\text{NH}_3\text{PbI}_3$ films can facilitate the diffusion of free carriers, thus leading to the enhancements of the charge transfer and separation efficiencies,^{15, 25} which play a vital role in improving the J_{sc} of the devices.⁴² In the present case, the crystallinity and the preferential orientation of samples C2, C4 and C6 are both increased compared with the sample C0, which implies the decrease of defects in the films. Therefore, the charge transfer and separation efficiencies in the corresponding devices should be effectively increased, which can substantially lead to the augment of the J_{sc} . To further verify this statement, we investigated the differences of charge dissociation behaviors in the prepared samples by means of the time-resolved PL decay measurements, and the corresponding results are presented in Figure 6. All the curves were fitted with two-component exponential decay function containing a fast decay and a slow decay processes. The fast decay process is considered to be the result of the quenching of free carriers in the $\text{CH}_3\text{NH}_3\text{PbI}_3$ domains through transport to TiO_2 , and the slow decay process to be the result of radiative recombination.¹⁵ As summarized in Table 2, the lifetime values of fast decay for the samples C2, C4 and C6 decrease and the corresponding weight fractions of fast decay increase with the increase of the recrystallization cycle compared with the sample C0. These results effectively verify the enhancement of charge dissociation properties of the $\text{CH}_3\text{NH}_3\text{PbI}_3$ films after recrystallization. In particular, the weight fraction related to the quenching of free carriers is up to 92% for the sample C6, indicating the extremely efficient charge transporting from the $\text{CH}_3\text{NH}_3\text{PbI}_3$ domains to TiO_2 . Therefore, the enhanced PCE of the devices with the samples C2, C4, and C6 can be

mainly attributed to the enhanced light absorption, the reduced shunting paths, and the increased charge transfer and separation efficiencies in the devices, as the results of the improved coverage and crystallinity of the $\text{CH}_3\text{NH}_3\text{PbI}_3$ films after recrystallization. Especially, for the sample C6, the homogeneous, pinhole-free and well crystallized $\text{CH}_3\text{NH}_3\text{PbI}_3$ layer can be realized, so the corresponding device exhibited the optimal performance.

It should be noted that the FF of all the devices presented in this work is relatively low. This is perhaps as a consequence of the HTM layer not being optimized (in terms of the layer thickness, the precursor solution concentration and the dopant levels). In fact, very little optimization work was carried out on these devices except for the $\text{CH}_3\text{NH}_3\text{PbI}_3$ layers. The work of optimization of the HTM layer is underway and it is conceivable that higher efficiency devices can be manufactured using this recrystallization procedure.

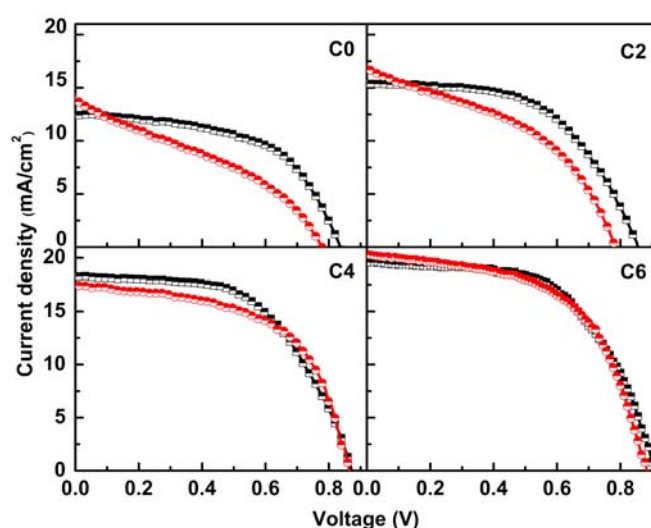


Figure 7 J-V curves measured at forward scan (FS, from short-circuit to open-circuit under the forward bias voltage) and reverse scan (RS, from open-circuit to short-circuit under the forward bias voltage) for the perovskite solar cells with the samples C0, C2, C4, and C6, respectively. Black square and red circle represent the RS and FS, respectively.

Recently, anomalous hysteresis phenomenon in the J-V test was widely observed in perovskite solar cells. Previous experimental results have shown that this phenomenon is depended on the properties of perovskite layer, the p- and n-type contact materials, and the device configuration.^{43,44} Because the devices based on the samples C0, C2, C4, and C6 have the same contact materials and configuration, the differences only came from the coverage and the crystallinity of the $\text{CH}_3\text{NH}_3\text{PbI}_3$ layers. So it is interesting to investigate the effects of these factors on the hysteresis phenomenon in the J-V test of the devices. As displayed in Figure 7, the devices with the samples C0, C2, C4, and C6 show different hysteresis behaviors, and the qualitative analysis of the hysteresis phenomenon is presented in Table S1. It can be seen that the device with the sample C0 exhibits serious hysteresis phenomenon, while for the devices with the samples C2, C4, and C6, the hysteresis become weak with the increase of the recrystallization cycle. Especially, for the sample C6 based device, the difference of J-V curves under FS and RS is extremely diminutive. These results suggest that recrystallization of the $\text{CH}_3\text{NH}_3\text{PbI}_3$ films by DMF vapor fumigation can effectively alleviate the hysteresis phenomenon in the J-V test of the devices, which is benefit to the devices' reliability in the practical applications. As revealed in the recent studies, the origin of the hysteresis phenomenon was ascribed to either the traps, the ferroelectric properties of the $\text{CH}_3\text{NH}_3\text{PbI}_3$ film and /or the ion migration induced by photo and/or electric field.⁴⁴ Here, the alleviation of the hysteresis phenomenon in the J-V test of the devices with the samples C2, C4, and C6 indicates that the origin of this phenomenon is most likely related to the formation of

traps induced by defects in the $\text{CH}_3\text{NH}_3\text{PbI}_3$ films.

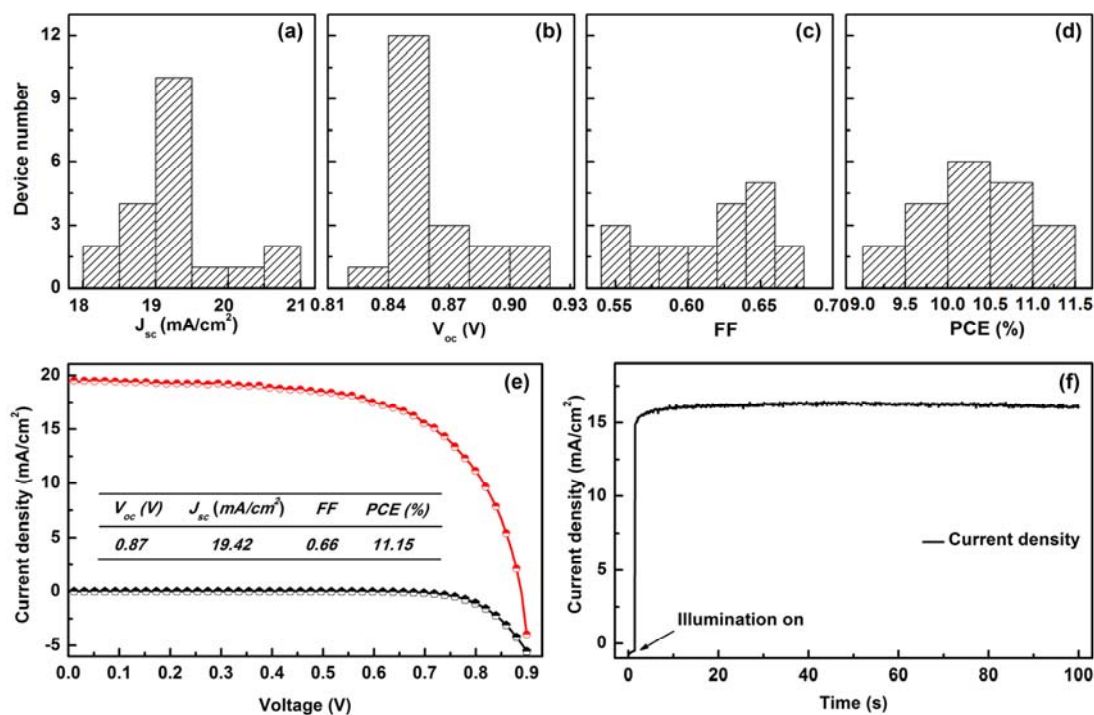


Figure 8 (a-d) Solar cell PV parameters statistics based on 20 solar cells with the C6 samples from four batches. (e) J-V curves measured under dark and simulated AM1.5 illumination for the optimal solar cell with the sample C6. Inset is the detailed performance parameters. (f) Photocurrent density as a function of time for the same solar cell held at a forward bias of 0.68 V. The cell was placed in the dark prior to the start of the measurement.

To further investigate the reproducibility of this recrystallization procedure in fabricating the mesostructured perovskite solar cells, we prepared twenty devices with the samples C6 from four batches, and the corresponding PV parameter statistics are shown in Figure 8 (a)-(d) and Table S2. The average V_{oc} , J_{sc} , FF, and PCE are 0.86 ± 0.05 V, 19.34 ± 1.50 mA cm⁻², 0.61 ± 0.07 , and $10.25 \pm 0.90\%$, respectively. Moreover, 70 % of the devices have the PCE above 10%. The excellent reproducibility can be attributed to the high uniformity of the $\text{CH}_3\text{NH}_3\text{PbI}_3$ films achieved by the recrystallization procedure, which is attractive for a large scale production of the perovskite solar cells. In particular, as presented in Figure 8(e), the

optimal performing solar cell shows the J_{sc} of 19.42 mA cm^{-2} , the V_{oc} of 0.87 V , the FF of 0.66 , and the PCE of 11.15% , which are comparable to that of previously reported high performance mesostructured or planar perovskite solar cells.^{12, 19, 45} To determine a more reliable PCE for the device, taking the hysteresis characteristics into consideration,⁴ the photocurrent was measured as a function of time at a forward bias near its maximum output power point. As exhibited in Figure 8(f), the photocurrent density stabilized within seconds to approximately 16.08 mA cm^{-2} , yielding stabilized PCE around 10.93% . This indicates that our test conditions (open-circuit to short-circuit under the forward bias voltage) provide a relatively accurate representation of the PV performance of the device while still result in a relative overestimation of the steady state power output by about 1.7% . These results indicate that the recrystallization procedure for realizing the uniform, full coverage, and high crystallinity $\text{CH}_3\text{NH}_3\text{PbI}_3$ films with excellent reproducibility can be a facile way to fabricate high performance perovskite solar cells.

4. Conclusions

In summary, we have demonstrated that the facile DMF vapor fumigation can induce the self-repair recrystallization of the one-step spin-coated $\text{CH}_3\text{NH}_3\text{PbI}_3$ films with dendritic structures to the uniform ones with full coverage and high crystallinity. The mesostructured perovskite solar cells based on these repaired $\text{CH}_3\text{NH}_3\text{PbI}_3$ films showed the reproducible optimal PCE of 11.15% and the average PCE of $10.25 \pm 0.90\%$, which are much better than that of the devices based on the non-repaired $\text{CH}_3\text{NH}_3\text{PbI}_3$ films. In addition, the hysteresis phenomenon in the J-V

test can also be effectively alleviated. The substantially enhanced PV performances can be mainly attributed to the enhanced light absorption, the reduced shunting paths, and the increased charge transfer and separation efficiencies in the optimized devices. Our work suggests a novel and attractive way to fabricate high performance perovskite solar cells.

Acknowledgements

This work was supported primarily by the national Natural Science Foundation of China (11174129 and 61377051), the National Basic Research Program of China (2011CB933303 and 2013CB632404), the Science and Technology Research Program of Jiangsu Province (BK20130053). We thank Prof. Xiaoyong Wang, Dr. Ligang Ma, Dr. Bihu Lv and Dr. Zhiqiang Wang for their informative discussions, experimental and technical assistance.

Notes and references

^aNational Laboratory of Solid State Microstructures & Eco-Materials and Renewable Energy Research Center (ERERC) at Department of Physics, Nanjing University, Nanjing 210093, P. R. China. E-mail: yutao@nju.edu.cn

^bCollaborative Innovation Center of Advanced Microstructures, Nanjing University, Nanjing 210093, P. R. China.

^cJiangsu Key Laboratory for Nano Technology, Nanjing 210093, P. R. China.

1. A. Hagfeldt, G. Boschloo, L. Sun, L. Kloo and H. Pettersson, *Chemical Reviews*, 2010, **110**, 6595-6663.
2. J. E. Coughlin, Z. B. Henson, G. C. Welch and G. C. Bazan, *Accounts of Chemical Research*, 2013, **47**, 257-270.
3. X. Lan, S. Masala and E. H. Sargent, *Nature Materials*, 2014, **13**, 233-240.
4. M. Xiao, F. Huang, W. Huang, Y. Dkhissi, Y. Zhu, J. Etheridge, A. Gray-Weale, U. Bach, Y. B. Cheng and L. Spiccia, *Angewandte Chemie International Edition*, 2014, **53**, 9898-9903.
5. A. Goetzberger and C. Hebling, *Solar Energy Materials and Solar Cells*, 2000, **62**, 1-19.
6. A. Kojima, K. Teshima, Y. Shirai and T. Miyasaka, *Journal of the American Chemical Society*, 2009, **131**, 6050-6051.

7. N. Park, *Nature Materials*, 2015, **14**, 140-141.
8. J. H. Noh, S. H. Im, J. H. Heo, T. N. Mandal and S. I. Seok, *Nano Letters*, 2013, **13**, 1764-1769.
9. F. Zuo, S. T. Williams, P.-W. Liang, C. C. Chueh, C. Y. Liao and A. K. Y. Jen, *Advanced Materials*, 2014, **26**, 6454-6460.
10. S. D. Stranks, G. E. Eperon, G. Grancini, C. Menelaou, M. J. P. Alcocer, T. Leijtens, L. M. Herz, A. Petrozza and H. J. Snaith, *Science*, 2013, **342**, 341-344.
11. E. J. Juarez-Perez, R. S. Sanchez, L. Badia, G. Garcia-Belmonte, Y. S. Kang, I. Mora-Sero and J. Bisquert, *The Journal of Physical Chemistry Letters*, 2014, **5**, 2390-2394.
12. M. M. Lee, J. Teuscher, T. Miyasaka, T. N. Murakami and H. J. Snaith, *Science*, 2012, **338**, 643-647.
13. J. You, Z. Hong, Y. Yang, Q. Chen, M. Cai, T.-B. Song, C.-C. Chen, S. Lu, Y. Liu, H. Zhou and Y. Yang, *ACS Nano*, 2014, **8**, 1674-1680.
14. D. B. Mitzi, in *Progress in Inorganic Chemistry*, John Wiley & Sons, Inc., 2007, pp. 1-121.
15. P.-W. Liang, C.-Y. Liao, C.-C. Chueh, F. Zuo, S. T. Williams, X.-K. Xin, J. Lin and A. K. Y. Jen, *Advanced Materials*, 2014, **26**, 3748-3754.
16. M. Grätzel, *Nature Materials*, 2014, **13**, 838-842.
17. G. E. Eperon, V. M. Burlakov, P. Docampo, A. Goriely and H. J. Snaith, *Advanced Functional Materials*, 2014, **24**, 151-157.
18. A. Dualeh, N. Tétreault, T. Moehl, P. Gao, M. K. Nazeeruddin and M. Grätzel, *Advanced Functional Materials*, 2014, **24**, 3250-3258.
19. H. S. Kim, C. R. Lee, J. H. Im, K. B. Lee, T. Moehl, A. Marchioro, S. J. Moon, R. Humphry-Baker, J. H. Yum, J. E. Moser, M. Grätzel and N. G. Park, *Scientific reports*, 2012, **2**, 591:1-7.
20. J. Burschka, N. Pellet, S.-J. Moon, R. Humphry-Baker, P. Gao, M. K. Nazeeruddin and M. Grätzel, *Nature*, 2013, **499**, 316-319.
21. M. Liu, M. B. Johnston and H. J. Snaith, *Nature*, 2013, **501**, 395-398.
22. Q. Chen, H. Zhou, Z. Hong, S. Luo, H.-S. Duan, H.-H. Wang, Y. Liu, G. Li and Y. Yang, *Journal of the American Chemical Society*, 2013, **136**, 622-625.
23. N. J. Jeon, J. H. Noh, Y. C. Kim, W. S. Yang, S. Ryu and S. I. Seok, *Nature Materials*, 2014, **13**, 897-903.
24. F. Huang, Y. Dkhissi, W. Huang, M. Xiao, I. Benesperi, S. Rubanov, Y. Zhu, X. Lin, L. Jiang, Y. Zhou, A. Gray-Weale, J. Etheridge, C. R. McNeill, R. A. Caruso, U. Bach, L. Spiccia and Y.-B. Cheng, *Nano Energy*, 2014, **10**, 10-18.
25. Y. Zhao and K. Zhu, *The Journal of Physical Chemistry C*, 2014, **118**, 9412-9418.
26. C. Zuo and L. Ding, *Nanoscale*, 2014, **6**, 9935-9938.
27. V. Mikli, J. Hiie, M. Viljus, R. Nisumaa, R. Traksamaa and U. Kallavus, *Thin Solid Films*, 2008, **516**, 7041-7045.
28. N. Romeo, A. Bosio, V. Canevari and A. Podestà, *Solar Energy*, 2004, **77**, 795-801.
29. A. Romeo, D. L. Bätzner, H. Zogg and A. N. Tiwari, *Thin Solid Films*, 2000, **361-362**, 420-425.
30. H. Rodriguez-Alvarez, R. Mainz, B. Marsen and H.-W. Schock, *Journal of Solid State Chemistry*, 2010, **183**, 803-806.
31. M. Krunks, V. Mikli, O. Bijakina and E. Mellikov, *Applied Surface Science*, 1999, **142**,

- 356-361.
32. D. Thomas, R. Mainz, H. Rodriguez-Alvarez, B. Marsen, D. Abou-Ras, M. Klaus, C. Genzel and H. W. Schock, *Thin Solid Films*, 2011, **519**, 7193-7196.
 33. K. Y. Law, *The Journal of Physical Chemistry*, 1985, **89**, 2652-2657.
 34. K. Tashiro and A. Yoshioka, *Macromolecules*, 2001, **35**, 410-414.
 35. J. P. Mercier, G. Groeninckx and M. Lesne, *Journal of Polymer Science Part C: Polymer Symposia*, 1967, **16**, 2059-2067.
 36. B.-w. Park, B. Philippe, T. r. Gustafsson, K. r. Sveinbjörnsson, A. Hagfeldt, E. M. Johansson and G. Boschloo, *Chemistry of Materials*, 2014, **26**, 4466-4471.
 37. H. Yu, F. Wang, F. Xie, W. Li, J. Chen and N. Zhao, *Advanced Functional Materials*, 2014, **24**, 7102-7108.
 38. Y.-J. Jeon, S. Lee, R. Kang, J.-E. Kim, J.-S. Yeo, S.-H. Lee, S.-S. Kim, J.-M. Yun and D.-Y. Kim, *Scientific Reports*, 2014, **4**, 6953:1-7.
 39. Y. Wu, A. Islam, X. Yang, C. Qin, J. Liu, K. Zhang, W. Peng and L. Han, *Energy & Environmental Science*, 2014, **7**, 2934-2938.
 40. H. Zhou, Q. Chen, G. Li, S. Luo, T.-b. Song, H.-S. Duan, Z. Hong, J. You, Y. Liu and Y. Yang, *Science*, 2014, **345**, 542-546.
 41. F. Hao, C. C. Stoumpos, Z. Liu, R. P. H. Chang and M. G. Kanatzidis, *Journal of the American Chemical Society*, 2014, **136**, 16411-16419.
 42. Z. Zhu, J. Ma, Z. Wang, C. Mu, Z. Fan, L. Du, Y. Bai, L. Fan, H. Yan, D. L. Phillips and S. Yang, *Journal of the American Chemical Society*, 2014, **136**, 3760-3763.
 43. H. S. Kim and N. G. Park, *The Journal of Physical Chemistry Letters*, 2014, **5**, 2927-2934.
 44. R. S. Sanchez, V. Gonzalez Pedro, J. W. Lee, N. G. Park, Y. S. Kang, I. Mora Sero and J. Bisquert, *The Journal of Physical Chemistry Letters*, 2014, **5**, 2357-2363.
 45. Z. Zhu, Y. Bai, T. Zhang, Z. Liu, X. Long, Z. Wei, Z. Wang, L. Zhang, J. Wang, F. Yan and S. Yang, *Angewandte Chemie International Edition*, 2014, **126**, 12779-12783.